



1  
2  
3  
4  
5  
6  
7  
8  
9  
10  
11  
12  
13  
14  
15  
16  
17  
18  
19  
20  
21  
22  
23

**A Passive Microwave Retrieval Algorithm with Minimal View Angle Bias:  
Application to the TEMPEST-D CubeSat Mission**

Richard M. Schulte<sup>1</sup>, Christian D. Kummerow<sup>1</sup>, Wesley Berg<sup>1</sup>, Steven C. Reising<sup>2</sup>, Shannon T. Brown<sup>3</sup>, Todd C. Gaier<sup>3</sup>, Boon H. Lim<sup>3</sup>, and Sharmila Padmanabhan<sup>3</sup>

<sup>1</sup>*Department of Atmospheric Science, Colorado State University, Fort Collins, Colorado*

<sup>2</sup>*Department of Electrical and Computer Engineering, Colorado State University, Fort Collins, Colorado*

<sup>3</sup>*Jet Propulsion Laboratory, California Institute of Technology, Pasadena, California*

*Corresponding author address:* Richard Schulte, Dept. of Atmospheric Science, Colorado State University, 1371 Campus Delivery, Fort Collins, CO 80523.  
E-mail: rschulte@atmos.colostate.edu

**Early Online Release:** This preliminary version has been accepted for publication in *Journal of Atmospheric and Oceanic Technology*, may be fully cited, and has been assigned DOI 10.1175/JTECH-D-19-0163.1. The final typeset copyedited article will replace the EOR at the above DOI when it is published.

24  
25  
26  
27  
28  
29  
30  
31  
32  
33  
34  
35  
36  
37  
38  
39  
40  
41  
42  
43  
44

## ABSTRACT

The rapid development of miniaturized satellite instrument technology has created a new opportunity to deploy constellations of passive microwave (PMW) radiometers to permit retrievals of the same Earth scene with very high temporal resolution to monitor cloud evolution and processes. In order for such a concept to be feasible, it must be shown that it is possible to distinguish actual changes in the atmospheric state from the variability induced by making observations at different Earth incidence angles (EIAs). To this end, we present a flexible and physical optimal estimation-based algorithm designed to retrieve profiles of atmospheric water vapor, cloud liquid water path, and cloud ice water path from cross-track PMW sounders. The algorithm is able to explicitly account for the dependence of forward model errors on EIA and atmospheric regime. When the algorithm is applied to data from the Temporal Experiment for Storms and Tropical Systems Technology Demonstration (TEMPEST-D) CubeSat mission, its retrieved products are generally in agreement with those obtained from the similar but larger Microwave Humidity Sounder instrument. More importantly, when forward model brightness temperature offsets and assumed error covariances are allowed to change with EIA and sea surface temperature, view angle-related biases are greatly reduced. This finding is confirmed in two ways: through a comparison with reanalysis data and by making use of brief periods in early 2019 during which the TEMPEST-D spacecraft was rotated such that its scan pattern was along-track, allowing dozens of separate observations of any given atmospheric feature along the satellite's ground track.

## 45 **1. Introduction**

46           Satellite-based passive microwave (PMW) radiometers have been used for several  
47 decades to measure atmospheric water vapor and bulk cloud properties such as total liquid water  
48 path and total ice water path (e.g. Wilheit and Chang 1980; Greenwald et al. 1993; Wentz 1997;  
49 Boukabara et al. 2010). PMW instruments also provide some of the most important observations  
50 for operational data assimilation (Geer et al. 2017). Recently, rapid advances in miniaturized  
51 satellite instrument technology have opened the door to making PMW measurements from U-  
52 Class satellites known as CubeSats. These much smaller satellite platforms could allow a larger  
53 number of satellites to be launched and many more PMW observations to be made, combining  
54 high temporal resolution that is unachievable from existing PMW satellite instruments with  
55 sensitivity to changes below the cloud top that is missing with geostationary visible and infrared  
56 measurements. This would provide both operational forecasters and data assimilation systems  
57 with additional useful information.

58           Moreover, while traditional PMW missions have focused on global mapping, cost-  
59 efficient PMW CubeSat missions facilitate the design of process-oriented studies that make use  
60 of constellations or “trains” of satellites to make repeated observations of atmospheric  
61 phenomena that occur on time scales of a few minutes to an hour or so (Ma et al. 2017). The  
62 proposed Temporal Experiment for Storms and Tropical Systems (TEMPEST) mission would  
63 consist of a cluster of 6-8 CubeSats carrying identical PMW radiometers and all in the same  
64 orbital plane. They would be separated by only a few minutes and thus could make repeated  
65 measurements of the same convective cells in order to better understand the evolution of these  
66 storm systems and the forcing and feedbacks between convection and mid-tropospheric water  
67 vapor. An illustration of the concept is presented in Figure 1.

68 To realize these potential applications of PMW CubeSat missions, it is necessary to  
69 demonstrate that they can provide science-quality measurements that are on par with those  
70 provided by similar instruments on larger satellites. For potential constellation “trains” designed  
71 to study cloud processes, one must also determine whether actual changes to the atmospheric  
72 state that occur over only a few minutes can be distinguished from the uncertainties involved in  
73 making measurements from two different satellites with different slant paths through the  
74 atmosphere (as illustrated in Figure 1, even two satellites in the same orbit plane will view the  
75 same spot on the Earth from slightly different angles because of the rotation of the Earth during  
76 the time between successive observations).

77 With the launch of the TEMPEST-D CubeSat, a technology demonstration mission  
78 currently on-orbit (Reising et al. 2018), it is now possible to begin addressing some of these  
79 questions directly. In particular, using yaw maneuvers performed by the TEMPEST-D  
80 spacecraft, we can assess view angle biases in a novel way, by comparing retrievals made by the  
81 same instrument at nearly the same time and over nearly the same area, but from different view  
82 angles. In this paper we apply the CSU 1DVAR retrieval algorithm (Schulte and Kummerow  
83 2019; hereafter SK19) to TEMPEST-D observations to retrieve total precipitable water (TPW),  
84 cloud liquid water path (LWP), and cloud ice water path (IWP) in order to answer two key  
85 questions:

- 86 1.) Do the TEMPEST-D measurements yield TPW, LWP, and IWP estimates that  
87 are consistent with those from the Microwave Humidity Sounder (MHS) class  
88 of PMW radiometers?

89           2.)           Do the TEMPEST-D estimates exhibit any bias as a function of view angle,  
90                           and are the view angle-related uncertainties small enough that real changes in  
91                           the atmospheric state can be distinguished from measurement uncertainty?

92           In Section 2 we further describe TEMPEST-D as well as our other data sources. Section 3  
93 provides a brief overview of the CSU 1DVAR algorithm and describes how we construct error  
94 covariance matrices and forward model brightness temperature offsets. In Section 4 we answer  
95 the key questions outlined above, and in Section 5 we discuss implications for future satellite  
96 missions.

97

## 98 **2. Data**

99           The TEMPEST-D satellite was launched on May 21, 2018 on a commercial resupply  
100 mission to the International Space Station and was successfully deployed into an orbit with an  
101 altitude of 400 km and inclination of  $51.6^\circ$  on July 13, 2018. The 6U (34 cm x 20 cm x 10 cm)  
102 CubeSat carries as its main payload a five-channel passive microwave radiometer operating in  
103 bands centered at 87, 164, 174, 178, and 181 GHz. The 87 GHz channel has quasi-vertical  
104 polarization (vertical polarization at nadir), while the other channels have quasi-horizontal  
105 polarization. Additional technical specifications are provided in Table 1, along with comparable  
106 values for the MHS radiometer, which operates at a similar set of frequencies onboard the  
107 MetOp-A, MetOp-B, MetOp-C, and NOAA-19 spacecraft. It should be noted that the mass and  
108 power of TEMPEST-D are far lower than those of operational PMW sensors, and also that  
109 TEMPEST-D has similar noise characteristics (as measured by NEDT) to MHS despite a  
110 significantly shorter integration time. For the same integration time, TEMPEST-D has lower  
111 noise than MHS.

112           Due to the roughly one-year period of time during which TEMPEST-D has been making  
113 measurements, as well as limitations in transmitting the collected data from the spacecraft to the  
114 ground, only limited data are available with which to evaluate the TEMPEST-D measurements  
115 and retrieval algorithm. This makes a comprehensive validation study difficult but does not  
116 prohibit our objectives; namely, demonstrating general agreement with MHS observations and  
117 examining view angle-related biases. In this study, we use one week of continuous data from  
118 Dec. 8-14, 2018 to meet the first objective and to calculate forward model bias corrections.

119           For the second objective, we make use of special periods during which the TEMPEST-D  
120 spacecraft was intentionally yawed by 92 degrees, thus providing along-track scanning during  
121 portions of the descending node of each orbit and nearly along-track scanning during the other  
122 periods (the exact degree to which the scans overlap is dependent both on the latitude and the  
123 direction of spacecraft motion). This dataset is to our knowledge the first of its kind from a  
124 spaceborne sensor and provides multiple observations of certain points on the Earth from wide-  
125 ranging view angles by the same instrument and at nearly the same time. All told, we have  
126 collected about 73 hours (or about 11.5 million retrieved pixels) of along-track observations,  
127 during January and April 2019.

128           Ancillary data (surface wind speeds, surface pressures, temperature profiles, and sea  
129 surface temperatures) used by the CSU 1DVAR retrieval algorithm are taken from the Goddard  
130 Earth Observing System Model, Version 5 (GEOS-5; Molod et al. 2012). The a priori water  
131 vapor profile used by the algorithm also comes from GEOS-5. GEOS-5 data is used (unlike  
132 reanalysis data as in SK19) in order to be able to run the retrieval in near real time. We examine  
133 coincident overpasses between TEMPEST-D and MHS, and compare the values retrieved by the  
134 TEMPEST-D algorithm to the corresponding MHS values from the Microwave Integrated

135 Retrieval System (MiRS; Boukabara et al. 2011) and to CSU 1DVAR retrievals run on the MHS  
136 data. MiRS Orbital Level-2 output is obtained from the NOAA Comprehensive Large Array-data  
137 Stewardship System (CLASS), and we use Version 11.2 of the algorithm. All satellites carrying  
138 an MHS sensor also have an Advanced Microwave Sounding Unit – A (AMSU-A), which has 15  
139 channels at frequencies ranging from 23.8 to 89.0 GHz and is primarily used for temperature  
140 sounding. It should be noted that radiances from this instrument are taken into account in the  
141 MiRS algorithm, but not in the CSU 1DVAR algorithm.

142

### 143 **3. Methods**

#### 144 *a. CSU 1DVAR*

145 The algorithm with which we retrieve TPW, LWP, and IWP from TEMPEST-D  
146 brightness temperatures ( $T_b$ ) is an extension of the optimal estimation algorithm developed in  
147 Duncan and Kummerow (2016). In brief, the 1DVAR or optimal estimation technique is an  
148 inverse method based on Bayes' Theorem; i.e.,

$$149 \quad P(\mathbf{x}|\mathbf{y}) = \frac{P(\mathbf{y}|\mathbf{x})P(\mathbf{x})}{P(\mathbf{y})} \quad (1)$$

150 In this case,  $\mathbf{y}$  is the measurement vector containing the observed  $T_b$  and  $\mathbf{x}$  is the state vector  
151 consisting of the atmospheric properties to be estimated (LWP, IWP, and the 3 leading principal  
152 components of the water vapor profile). Given radiometer observations  $\mathbf{y}$ , we wish to find the  
153 value of  $\mathbf{x}$  for which the posterior probability  $P(\mathbf{x}|\mathbf{y})$  is maximized. If we consider  $P(\mathbf{y})$  to be a  
154 normalizing factor, then this amounts to maximizing the product of the a priori probability of a  
155 given state,  $P(\mathbf{x})$ , with the probability of measuring the set of  $T_b$  if  $\mathbf{x}$  were indeed the state of the  
156 atmosphere,  $P(\mathbf{y}|\mathbf{x})$ . The relationship between  $\mathbf{x}$  and  $\mathbf{y}$  can be generalized by

157 
$$\mathbf{y} = \mathbf{f}(\mathbf{x}, \mathbf{b}) + \boldsymbol{\varepsilon}, \quad (2)$$

158 where  $\mathbf{f}$  is a forward model based on radiative transfer theory. The forward model requires  
159 additional information besides the parameters given in  $\mathbf{x}$  in order to be able to calculate  
160 simulated  $T_b$  (such as the temperature profile, the surface wind speed, the cloud structure, etc.),  
161 and these various assumptions are represented by the vector  $\mathbf{b}$ .  $\boldsymbol{\varepsilon}$  is an error term containing  
162 uncertainties due to sensor noise, errors in the forward model, and uncertainties in the ancillary  
163 parameters,  $\mathbf{b}$ . In theory, the forward modeled brightness temperatures,  $\mathbf{f}(\mathbf{x}, \mathbf{b})$ , should agree  
164 with the satellite measurements  $\mathbf{y}$  within the model and sensor error estimates given by  $\boldsymbol{\varepsilon}$ . The  
165 aim of the 1DVAR algorithm is to find the most likely state vector  $\mathbf{x}$ , given measurements  $\mathbf{y}$ ,  
166 prior knowledge about the state of the atmosphere, and proper error estimates.

167 It can be shown (Rodgers 2000) that, under the assumption of Gaussian errors in the  
168 assumed a priori state and in observed and forward modeled  $T_b$ , maximizing the numerator on  
169 the right hand side of Equation 1 is equivalent to minimizing the cost function,  $\Phi$ :

170 
$$\Phi = (\mathbf{x} - \mathbf{x}_a)^T \mathbf{S}_a^{-1} (\mathbf{x} - \mathbf{x}_a) + [\mathbf{y} - \mathbf{f}(\mathbf{x}, \mathbf{b})]^T \mathbf{S}_y^{-1} [\mathbf{y} - \mathbf{f}(\mathbf{x}, \mathbf{b})]. \quad (3)$$

171 The first term in  $\Phi$  indicates how far a potential solution is from the assumed a priori state,  $\mathbf{x}_a$ .  
172 This difference is weighted by the assumed errors in the a priori parameters and their  
173 covariances, as described by the a priori covariance matrix  $\mathbf{S}_a$ . The second term is a measure of  
174 the difference between observed and forward modeled  $T_b$ , and it contains a second error  
175 covariance matrix, the  $\mathbf{S}_y$  matrix, which describes the uncertainties in both the observations and  
176 the forward model. The Gauss-Newton method is used to iteratively solve for the value of  $\mathbf{x}$  at  
177 which the gradient of the cost function,  $\nabla_{\mathbf{x}} \Phi$ , is equal to zero.

178 We use the same forward model as in SK19, the key components being Version 5.3 of the  
179 Monochromatic Radiative Transfer Model (MonoRTM; Clough et al. 2005) for calculating

180 absorption coefficients and the FASTEM6 model of ocean surface emissivity (Kazumori and  
181 English 2015). We also make the same assumptions as in SK19 about cloud composition and  
182 height. To summarize, cloud water is distributed evenly between the pressure levels of 800 hPa  
183 and 925 hPa, with an assumed monodisperse drop size distribution (DSD) of spherical cloud  
184 droplets with radii of 12  $\mu\text{m}$ . Ice particles are likewise distributed evenly between 300 and 400  
185 hPa, with a parameterization of the ice particle size distribution which comes from Field et al.  
186 (2007), and scattering calculated according to a database of single-scattering properties at  
187 microwave frequencies for various ice crystal habits (Liu 2008) as well as an associated database  
188 for larger aggregates of ice crystals (Nowell et al. 2013). Assumptions made with regard to ice  
189 particles can greatly impact modeled  $T_b$  (Kulie et al. 2010). While we believe the assumptions  
190 made in our algorithm strike a reasonable balance between simplicity and accuracy, we  
191 acknowledge the substantial uncertainties involved. We direct the reader to SK19 for a  
192 quantification of the uncertainties and biases created by these forward model assumptions (see in  
193 particular Figures 1 and 2).

194

#### 195 *b. Construction of Covariance Matrices and Forward Model Offsets*

196 The 1DVAR retrieval solution can be quite sensitive to the error covariance matrices  $\mathbf{S}_a$   
197 and  $\mathbf{S}_y$  (Duncan and Kummerow, 2016), so it is important that the assumed uncertainties specified  
198 in these matrices are carefully calculated and not just ad-hoc guesses.  $\mathbf{S}_a$  uncertainties are  
199 estimated from covariances between state vector values in ERA5 reanalysis data, following SK19.  
200 More interesting is the calculation of the  $\mathbf{S}_y$  matrix, as well as forward model  $T_b$  offsets that are  
201 meant to account for systematic biases in the forward model and/or the PMW radiometer.

202 We start with TEMPEST-D observed  $T_b$  from Dec. 8-14, 2018. We match ERA5  
203 atmospheric profiles, at their full native vertical resolution, to the TEMPEST-D pixels, and  
204 calculate simulated TEMPEST-D  $T_b$  using the same radiative transfer model used in the retrieval  
205 forward model. Pixels for which ERA5 indicates precipitation are excluded. Next, we create a  
206 second set of simulated observations; however, this time we reduce the accuracy of the simulated  
207  $T_b$  by making the same assumptions made in the retrieval algorithm. The vertical resolution is  
208 reduced, all of the cloud water and ice is constrained to lie within the levels specified in the  
209 retrieval (given above), and the vertical profiles of water vapor are simplified to that which can be  
210 best described by only three principal components (PCs; see SK19 for details on how the forward  
211 model handles the water vapor profile). We also add random perturbations to the surface  
212 temperature and wind speed, the salinity, and the temperature profile, to mimic the real-world  
213 uncertainty present in the values used for the forward model's ancillary and assumed parameters.

214 By comparing these two sets of simulated  $T_b$ , one from a detailed representation of the  
215 atmosphere and the other from the simplified representation of the retrieval forward model, we  
216 can estimate the channel uncertainties related to the forward model. The  $S_y$  matrix is formed by  
217 calculating the covariances of the simulated minus simulated  $T_b$  differences, and then adding the  
218 TEMPEST-D noise equivalent differential temperature (NEDT) for each channel, which are  
219 assumed to be uncorrelated, to the diagonal elements of the matrix. In doing so we assume that  
220 instrument channel errors are uncorrelated, though it is true that some types of instrument errors,  
221 such as the error in specifying the hot-load temperature, are correlated across channels.

222 Each TEMPEST-D pixel without precipitation is binned based on the sea surface  
223 temperature for the pixel (SST) and the earth incidence angle (EIA) between the radiometer  
224 boresight and the local vertical at the location of the pixel. We use 33 SST bins (in 1 K

225 increments from 273 K to 305 K) and 30 angle bins (in 4 degree increments from  $-60^\circ$  to  $60^\circ$ ).  
226 Then a separate  $\mathbf{S}_y$  matrix is calculated for each bin, following SK19. Our justification for this is  
227 that the nature of the forward model errors is dependent both on the atmospheric regime (for  
228 which we use SST as a proxy) and on the view angle being considered. For example, colder SSTs  
229 are generally associated with reduced total column water vapor. The TEMPEST-D 87 GHz  
230 channel is more sensitive to the surface when there is less water vapor, making that channel's  
231 uncertainties more sensitive to SST, wind speed, and emissivity model errors and thus increasing  
232 the channel uncertainty. This can be seen in Figure 2. Likewise, when the EIA is large the slant  
233 path through the atmosphere will be longer and there will be less sensitivity to uncertainties in  
234 surface parameters. A larger EIA also corresponds to a larger instantaneous field of view, which  
235 can further change the nature of forward model errors due to field-of-view inhomogeneities. For  
236 the higher frequency channels, the general trend is that, the more sensitive the channel is to the  
237 upper troposphere, the larger the uncertainty. Thus the uncertainty increases both as one moves  
238 closer in frequency to the 183 GHz water vapor absorption line and as the EIA increases. The  
239 increased uncertainty is likely due to both the relatively coarse resolution of the upper troposphere  
240 in the forward model as well as the simplistic way in which ice clouds are represented. SK19  
241 found that accounting for these EIA and SST dependent changes in the  $\mathbf{S}_y$  matrix, when applying  
242 the CSU 1DVAR retrieval to MHS observations, made a small but significant difference in the  
243 final retrieved TPW values and led to a greater consistency across the MHS scans.

244         This procedure of estimating  $\mathbf{S}_y$  accounts for many of the most significant sources of  
245 forward model error, particularly for clear sky conditions where scattering is not a factor. It also  
246 accounts for the random component of instrument error, through the addition of the channel  
247 NEDT. However, it does not account for systematic biases that might exist between the observed

248 and forward modeled  $T_b$ . These biases could exist for many reasons, and could be related to  
249 either instrument or forward model errors. For example, errors in the measurement of the  
250 calibration load temperature, or the intrusion of microwave radiation from a non-Earth source  
251 such as the spacecraft itself, could lead to an instrument bias. On the other hand, all of the  
252 sources of forward model error considered in the  $\mathbf{S}_y$  calculation, as well as harder-to-quantify  
253 uncertainties such as absorption model and emissivity model errors, could contribute to a  
254 forward model bias. While disentangling all of these effects is difficult, estimating their  
255 cumulative impact is somewhat easier, and we correct for them by applying  $T_b$  offsets, or bias  
256 corrections, to the TEMPEST-D observations before processing them.

257         To calculate these  $T_b$  offsets, we compare the observed TEMPEST-D  $T_b$  from Dec. 8-14,  
258 2018 with the set of  $T_b$  simulated from ERA5 using the simplified model of the atmosphere. As  
259 mentioned above, the nature of forward model errors for each channel is somewhat dependent on  
260 the EIA and the SST regime being considered. This is true not only for the magnitude of the  
261 error variances and covariances (i.e. the information in  $\mathbf{S}_y$ ) but also for systematic biases.  
262 Likewise, it is reasonable to suspect that instrument biases might also be dependent on scan  
263 position (John et al. 2013) or scene temperature (which will to some degree be correlated with  
264 SST). Thus, we bin the bias corrections by EIA and SST, just as we do the  $\mathbf{S}_y$  covariances. For  
265 each SST/EIA combination bin, we calculate the median observed minus simulated  $T_b$  from the  
266 observation period. We use the median rather than the mean because the median is less sensitive  
267 to outlier values that can result, for example, if ERA5 misplaces a frontal system relative to  
268 where the  $T_b$  signature suggests it should be. The median values are then smoothed in EIA-SST  
269 space using a Gaussian convolution filter, and it is these smoothed values that are used as  
270 forward model offsets in the CSU 1DVAR retrieval. That is, the appropriate offset for a given

271 pixel's EIA and SST is added to the output of the forward model before comparing it with the  
272 observed  $T_b$ . The forward model offsets for each TEMPEST-D channel are shown in Figure 3,  
273 and it is clear that the offsets are complicated functions of both EIA and SST. This method of  
274 calculating offsets does risk incorporating biases that might be present in ERA5 into the final  
275 parameters retrieved from TEMPEST-D  $T_b$  by the CSU 1DVAR algorithm. However, since  
276 possible ERA5 biases will be location dependent rather than EIA dependent, this does not deter  
277 our primary objective of evaluating the consistency of TEMPEST-D retrievals as a function of  
278 EIA.

279

## 280 **4. Results**

### 281 *a. Consistency with MHS*

282 The MHS radiometer, with a set of channels that are quite similar to TEMPEST-D, is a  
283 natural instrument against which to compare observations. One way to assess the quality of  
284 TEMPEST-D observations is to compare TEMPEST-D  $T_b$  to MHS  $T_b$  using the so-called  
285 “double difference method.” This method shows that TEMPEST-D  $T_b$  are consistent with MHS  
286  $T_b$  to within about 1 K (slightly larger differences exist at the 164 GHz channel, because of band  
287 mismatches and surface emissivity sensitivity), and that the calibration differences are stable  
288 with time (Berg et al. 2019).

289 Another way to evaluate the consistency with MHS is to look at retrieved products. MHS  
290 instruments are in sun-synchronous polar orbits, which means that the field of view of  
291 TEMPEST-D coincides with the field of view of each MHS radiometer twice per orbit. Figure 4  
292 shows an example of such an overpass from Dec. 9, 2018. In this case, TEMPEST-D made  
293 observations over the Western Pacific Ocean around 11:24 UTC that were nearly coincident with

294 observations from the MetOp-B satellite. Figure 4 compares the TPW, LWP, and IWP retrieved  
295 from TEMPEST-D by the CSU 1DVAR algorithm to that retrieved from MetOp-B by the MiRS  
296 algorithm. The top plots show the TEMPEST-D values with the MiRS swath in the background,  
297 and in the bottom plots the order is reversed. The two products are in broad agreement. They  
298 agree quite well on the placement of liquid phase clouds to the south of Japan, for instance, as  
299 well as the existence of ice particles north of Papua New Guinea. The main features of the water  
300 vapor field are the same, and there are no sharp gradients in TPW when the two retrieved swaths  
301 are plotted on top of each other.

302         Looking at all TEMPEST-D / MHS near-coincident observations from the Dec. 8-14  
303 period, the story is much the same. To identify all such observations, the data were gridded on an  
304 Earth-fixed quarter-degree grid (necessary because the MHS and TEMPEST-D footprints and  
305 ground tracks do not match), and observations taken within 5 minutes of each other were  
306 included for analysis. This resulted in 17,869 instances of matched pixels that were over the  
307 ocean and had valid data for both TEMPEST-D and MiRS. Summary statistics for the difference  
308 in retrieved TPW and LWP are given in Table 2, and scatterplots between TEMPEST-D and  
309 MiRS values are shown in Figures 5 and 6 for TPW and LWP, respectively. Due to the time  
310 period considered and the inclination of the TEMPEST-D and MHS orbits, most of the near-  
311 coincident observations occurred in the mid-latitudes, so we caution that the relationships  
312 presented here might be different in other regimes.

313         Retrieved TPW is correlated quite highly, with a correlation coefficient of 0.976 and a  
314 standard deviation of the difference between of the two values of 2.87 mm. TEMPEST-D TPW  
315 is biased low compared to MiRS TPW; however, it should be noted that SK19 found that MiRS  
316 TPW estimates were biased high compared to ground-based SuomiNet estimates, so this puts

317 TEMPEST-D estimates more in line with SuomiNet. The correlation between LWP estimates is  
318 not as strong ( $r=0.692$ ), as evident in Figure 6, but this is to be expected. LWP is inherently  
319 harder to retrieve (it is very hard to radiometrically distinguish cloud water from rain water, for  
320 example) and can vary dramatically on small spatial scales. Even if both the MiRS and  
321 TEMPEST-D retrieval algorithms were perfect, one would expect to see considerable differences  
322 in retrieved LWP for pixels up to a quarter degree apart in space and up to five minutes apart in  
323 time.

324

#### 325 *b. Consistency Across Scan*

326 In SK19, it was shown that MiRS TPW estimates from MHS instruments tended to be  
327 higher near nadir and drop off at large view angles, and that a similar pattern was seen in CSU  
328 1DVAR TPW estimates from cross-track instruments when constant (i.e. no SST or EIA  
329 dependence) error covariance assumptions were used. Since MiRS employs scan position-based  
330  $T_b$  offsets meant to account for instrument errors, and the CSU 1DVAR was run using inter-  
331 calibrated MHS  $T_b$  that should theoretically have no scan asymmetry, it was speculated that this  
332 pattern might be the result of shared forward model errors (such as algorithms' use of the same  
333 surface emissivity model). When the CSU 1DVAR algorithm was re-run using a variable  $S_y$   
334 matrix and forward model offsets that changed based on EIA and SST, this across-scan bias was  
335 almost totally eliminated, even when the algorithm was run on data from different time periods  
336 and from satellites other than the one used to calculate the forward model adjustments. This  
337 supported the hypothesis that forward model errors were mostly responsible for the asymmetry,  
338 and that view angle-related biases could be corrected by accounting for these forward model  
339 errors (even if the specific causes of the forward model errors remained hard to diagnose).

340 Here we perform similar experiments using the TEMPEST-D instrument, and we once  
341 again find that the methodology presented in Section 3b is able to largely mitigate view angle  
342 related biases. One way to address this question is to compare TEMPEST-D retrieved TPW as a  
343 function of EIA with reanalysis data. We use the European Center for Medium-Range Weather  
344 Forecasts' reanalysis product, ERA5 (ECMWF 2017), for this purpose. Considering that ERA5  
345 incorporates a physically based atmospheric model, and that TEMPEST-D observations are not  
346 assimilated into ERA5, ERA5 TPW errors should be independent of TEMPEST-D view angle.  
347 Thus, when comparing a retrieved product to ERA5, one would expect to find a nearly constant  
348 average difference with respect to EIA. Figure 7 shows the result of this sort of comparison for  
349 all TEMPEST-D pixels from Dec. 8-14, and confirms that the difference with respect to EIA is  
350 nearly flat. Also shown for comparison is the average (MetOp-B) MiRS TPW bias compared to  
351 ERA5 as a function of EIA, and the same edge-of-scan roll-off found in SK19 is evident.

352 However, with the unique yaw maneuver dataset from TEMPEST-D, it is possible to  
353 examine possible view angle-related biases more directly than in SK19. While the satellite was  
354 in the along-track scanning mode, the TEMPEST-D instrument viewed the same locations many  
355 times in quick succession. These views can be categorized according to EIA to examine the  
356 consistency of retrieved products in a much more direct way than was possible in SK19. Figure 8  
357 shows an example of this. A TEMPEST-D nadir-viewing pixel (located at the spot marked "X"  
358 in Figure 9) is taken as the reference point and all preceding or subsequent observations whose  
359 center field-of-view point is within 10 km of the center of the reference pixel are considered to  
360 be coincident. Figure 8 shows that the retrieved TPW and LWP (IWP is negligible in this case)  
361 are quite consistent for all retrievals, with no noticeable dependence on EIA.

362           This particular case study was chosen in part because it occurred simultaneous with a  
363 MetOp-B overpass with MHS observations. The CSU 1DVAR algorithm was also run on the  
364 MHS pixel closest to the reference point for comparison. This value (which was associated with  
365 an EIA of approximately  $27^\circ$ ) is shown by the constant red line in Figure 8. One of the  
366 advantages of the optimal estimation framework is that explicit error estimates are provided by  
367 the posterior error covariance matrix. The red dashed lines in Figure 8 represent the  $\pm 1$  standard  
368 deviation uncertainty ranges for the MHS-based estimates. The first thing to note is that the  
369 TEMPEST-D estimates agree reasonably well with the MHS estimates. This is especially true  
370 considering that the TEMPEST-D and MHS footprints do not align perfectly, and that the  
371 observations were taken a few minutes apart from each other. Additionally, the variation  
372 between the different TEMPEST-D estimates is smaller than the uncertainty associated with the  
373 single MHS estimate. This suggests that the retrieval uncertainty is driven more by uncertain  
374 forward model assumptions (which are common to all observations) than by instrument  
375 uncertainties or view angle differences.

376           Taking a larger view, Figure 9 shows the full context in which this comparison was  
377 made. The TEMPEST-D ground track is plotted on top of the coincident MHS swath, with CSU  
378 1DVAR retrieved values of TPW and LWP. TEMPEST-D crosses a sharp water vapor gradient  
379 near ( $50^\circ\text{S}$ ,  $30^\circ\text{E}$ ) and also passes over two significant cloud clusters. The middle panels in  
380 Figure 9 show all TEMPEST-D pixels located within 10 km of the red ground track, categorized  
381 by EIA and longitude and colored according to the retrieved value of TPW or LWP. Matching  
382 the colors in these panels to the corresponding locations in the top panels, it is seen that there is  
383 good agreement between the TEMPEST-D and MHS observations, particularly with regard to  
384 the sharp water vapor gradient and the location of clouds. The vertical “stripes” in these plots

385 show that the retrieved values at a given location tend to be very consistent as a function of EIA.  
386 The consistency with MHS retrievals and between retrievals taken at different view angles is also  
387 apparent when looking at the bottom panels, which plot the spread of TEMPEST-D values  
388 retrieved along the ground track at all view angles compared with MHS retrieved values for the  
389 MHS pixels closest to the ground track. From these plots one can see that the TEMPEST-D  
390 retrievals mostly fall within the MHS error bounds, and also that the spread of the TEMPEST-D  
391 retrievals is smaller than the overall uncertainty in the MHS retrievals.

392 Finally, we consider the entirety (all 73 hours) of the TEMPEST-D yaw maneuver  
393 dataset. Observations are binned into 4-degree bins according to their EIA, and the retrieved  
394 TPW and LWP are compared with those retrieved by TEMPEST-D at the same point at nadir (if  
395 no such observation exists within 5 km of the pixel being considered, that pixel is excluded from  
396 the analysis). Figure 10 shows the median difference between these observations and  
397 observations of the same location at nadir. The median difference is nearly independent of EIA  
398 for TPW, and while the relationship for LWP is slightly noisier, the relationship with EIA is also  
399 largely flat.

400 Figure 10 also shows the resulting biases when the CSU 1DVAR algorithm is run on the  
401 TEMPEST-D yaw maneuver data without variable forward model  $T_b$  offsets or error covariance  
402 matrices. The mean  $T_b$  offset and average  $S_y$  matrix, across all EIA and SST bins, are used  
403 instead. In this case, there are clear patterns in the TPW and LWP biases with respect to EIA. On  
404 the TPW side, there is both the familiar edge-of-scan roll-off that is seen in the MiRS data as  
405 well as a left-to-right asymmetry. This is probably the result of an instrument asymmetry, as a  
406 similar pattern is seen when comparing TEMPEST-D 87 GHz  $T_b$  to collocated MHS 89 GHz  $T_b$ ,  
407 and the TEMPEST-D  $T_b$  have not been calibrated in any way except for the process of

408 calculating forward model offsets. Meanwhile, the LWP plot shows that, under this scenario,  
409 LWP becomes biased high at high view angles, perhaps to compensate for missing TPW. A third  
410 experiments was run in which  $S_y$  matrices and forward model offsets were binned by EIA, but  
411 not by SST. This is similar to the current set-up of MiRS. In this case, the edge-of-scan bias is  
412 reduced but not eliminated. This demonstrates that, because the nature of EIA-dependent forward  
413 model errors is different for different atmospheric regimes, nuanced error assumptions that take  
414 into account both EIA and atmospheric conditions are necessary to fully eliminate view angle  
415 related biases. In a final experiment, the forward model offsets were allowed to vary based upon  
416 both EIA and SST, but the  $S_y$  matrix was held constant. Consistent with SK19, the variable  
417 forward model offsets are primarily responsible for improving the across-scan consistency;  
418 however, the variable  $S_y$  matrix does play a small role as well.

419

## 420 **5. Conclusion**

421 TEMPEST-D observations show that CubeSat missions offer the potential to greatly  
422 increase the frequency of PMW observations across the globe, for use in forecasting, data  
423 assimilation, and process studies. TEMPEST-D measurements appear to be of similar quality to  
424 MHS measurements, as evidenced both by the consistency between TEMPEST-D and MHS  $T_b$   
425 and (as demonstrated in this study), the consistency in atmospheric parameters retrieved from  
426 TEMPEST-D by the CSU 1DVAR algorithm and those retrieved from MHS instruments. This is  
427 true both of MiRS retrievals and of CSU 1DVAR retrievals performed on MHS data.

428 One important consideration when it comes to cross-track scanning PMW instruments  
429 like TEMPEST-D or MHS is the potential for across-scan biases in retrieved parameters. This  
430 becomes critical as the time sampling of PMW observations increases to explore changes in an

431 atmospheric parameter that occur between observations. In order for actual changes from one  
432 observation to another (made with a different satellite and likely with a different viewing  
433 geometry) to be detected, one must have confidence that differences in retrieved values are due  
434 to actual physical changes and not due to forward model errors that depend on view angle.

435         The CSU 1DVAR algorithm has been shown to have near-zero view angle bias when it  
436 comes to the retrieval of TPW and LWP from TEMPEST-D observations. This is true both when  
437 comparing TEMPEST-D retrieved values to reanalysis estimates and when looking directly at  
438 the same location many times with the TEMPEST-D instrument when the satellite was  
439 performing yaw maneuvers. The elimination of view angle-dependent errors is achieved only  
440 when assumptions about both systematic and random errors are allowed to change based on SST  
441 regime and instrument EIA. Systematic errors are accounted for in the forward model  $T_b$  offsets  
442 while random errors are specified in the error covariance matrix  $S_y$ . The physical justification for  
443 doing this is that the nature of forward model errors will change with atmospheric regime and  
444 EIA, as demonstrated in SK19. When constant error assumptions are used instead, a clear EIA-  
445 related pattern is seen in the TPW and LWP biases. A similar TPW pattern is seen in MiRS  
446 retrievals on MHS data, suggesting that there might be forward model errors that are common to  
447 both algorithms. Other optimal estimation based retrieval algorithms might benefit from adopting  
448 the approach presented here of varying error assumptions based on SST and EIA. While we have  
449 used SST (which is correlated with TPW) as a proxy for atmospheric regime, other methods  
450 including atmospheric air mass could be explored.

451         The lessons learned through the development of the CSU 1DVAR algorithm about view  
452 angle related biases for cross-track scanning PMW radiometers could be useful for the upcoming  
453 TROPICS mission (Blackwell et al. 2018). TROPICS will consist of six CubeSats with PMW

454 radiometers measuring at similar frequencies to TEMPEST-D (with the addition of several  
455 channels near the 118.75 GHz oxygen absorption line) that will be launched into three different  
456 orbital planes, providing rapid-refresh PMW measurements in the tropics. With refresh times  
457 under one hour in some cases, it will be important to consider the impact different view angles  
458 could have on observations and to mitigate view angle biases as much as possible. This work  
459 could also be of interest to the data assimilation community, since it is possible that the radiative  
460 transfer models used to assimilate PMW satellite observations could have similar view angle  
461 dependent errors to the errors present in the CSU 1DVAR forward model.

462         We acknowledge that one limitation of the study is that the same time period used to  
463 calculate the forward model offsets and error covariance matrix is also used to test the retrieval  
464 algorithm against MiRS. However, good retrieval results are also seen during the January and  
465 April along-track scanning periods, using the same offsets and covariances. In addition, the  
466 concentration of TEMPEST-D / MHS overpasses in the mid-latitudes on the dates studied  
467 precludes a more thorough analysis of possible regional biases. As more TEMPEST-D data are  
468 collected, it will become possible to conduct even more rigorous statistical analyses and explore  
469 seasonal and regional dependencies.

470         Finally, we note that the TEMPEST-D yaw maneuver data used in this study offer many  
471 possible avenues for further exploration. The TEMPEST-D along-track observations from clear-  
472 sky areas might be able to yield some insight into possible angle-dependent surface emissivity  
473 model errors near 87 and 164 GHz. In addition, looking at the same scenes from multiple angles  
474 gives additional information that could be used to investigate the vertical structure of water vapor  
475 and clouds. The CSU 1DVAR algorithm framework is flexible enough that it could be modified

476 to include multi-angle observations. The TEMPEST-D data are publicly available at  
477 <https://tempest.colostate.edu/data>.

478

479 *Acknowledgments.* The authors thank Dr. David Duncan for numerous helpful  
480 discussions throughout the development of the CSU 1DVAR algorithm, and the entire  
481 TEMPEST-D team at Colorado State University, the Caltech Jet Propulsion Laboratory, and  
482 Blue Canyon Technologies for their work in building and launching TEMPEST-D. The work  
483 was supported by NASA Earth Venture Program Grant NNX15AP56G.

484

485 **References**

- 486 Blackwell, W. J., and coauthors, 2018: An overview of the TROPICS NASA Earth venture  
487 mission. *Quart. J. Roy. Meteor. Soc.*, **144** (Suppl. 1), 16-26,  
488 <https://doi.org/10.1002/qj.3290>
- 489 Berg, W., and coauthors, 2019: Demonstrating the viability of the TEMPEST-D CubeSat  
490 radiometer for science applications, *IGARSS 2019 – 2019 IEEE International Geoscience  
491 and Remote Sensing Symposium*, Yokohama, Japan.
- 492 Boukabara, S.-A., K. Garrett, and W. Chen, 2010: Global coverage of total precipitable water  
493 using a microwave variational algorithm. *IEEE Trans. Geosci. Remote Sens.*, **48**, 3608-  
494 3621, <https://doi.org/10.1109/TGRS.2010.2048035>.
- 495 Boukabara, S.-A., and coauthors, 2011: MiRS: An all-weather 1DVAR satellite data assimilation  
496 and retrieval system. *IEEE Trans. Geosci. Remote Sens.*, **49**, 3249-3272, [https://doi.org/  
497 10.1109/TGRS.2011.2158438](https://doi.org/10.1109/TGRS.2011.2158438).
- 498 Clough, S. A., and coauthors, 2005: Atmospheric radiative transfer modeling: A summary of the  
499 AER codes. *J. Quant. Spectrosc. Radiat. Transfer*, **91**, 233-244, [https://doi.org/10.1016/  
500 j.jqrst.2004.05.058](https://doi.org/10.1016/j.jqrst.2004.05.058)
- 501 Duncan, D. I., and C. D. Kummerow, 2016: A 1DVAR retrieval applied to GMI: Algorithm  
502 description, validation, and sensitivities. *J. Geophys. Res.: Atmos.*, **121**, 7415-7429,  
503 <https://doi.org/10.1002/2016JD024808>.
- 504 European Center for Medium Range Weather Forecasts, 2017: ERA5 Reanalysis. National  
505 Center for Atmospheric Research, Computational and Information Systems Laboratory,  
506 accessed 1 June 2018, <https://doi.org/10.5065/D6X34W69>.

507 Field, P. R., A. J. Heymsfield, and A. Bansemer, 2007: Snow size distribution parameterization  
508 for midlatitude and tropical ice clouds. *J. Atmos. Sci.*, **64**, 4346-4364, [https://doi.org/  
509 10.1175/2007JAS2344.1](https://doi.org/10.1175/2007JAS2344.1).

510 Geer, A. J., and coauthors, 2017: The growing impact of satellite observations sensitive to  
511 humidity, cloud, and precipitation. *Q. J. Royal Meteorol. Soc.*, **143**, 3189-3206,  
512 <https://doi.org/10.1002/qj.3172>.

513 Greenwald, T. J., G. L. Stephens, T. H. Vonder Haar, and D. L. Jackson, 1993: A physical  
514 retrieval of cloud liquid water over the global oceans using special sensor microwave /  
515 imager (SSM/I) observations. *J. Geophys. Res.: Atmos.*, **98**, 18,471-18,478,  
516 <https://doi.org/10.1029/93JD00339>.

517 John, V. O., G. Holl, N. Atkinson, and S. A. Buehler, 2013: Monitoring scan asymmetry of  
518 microwave humidity sounding channels using simultaneous all angle collocations  
519 (SAACs). *J. Geophys. Res.: Atmos.*, **118**, 1536-1545, [https://doi.org/10.1002/  
520 jgrd.50154](https://doi.org/10.1002/jgrd.50154),2013.

521 Kazumori, M., and S. J. English, 2015: Use of the ocean surface wind direction signal in  
522 microwave radiance assimilation. *Quart. J. Roy. Meteor. Soc.*, **141**, 1354-1375,  
523 <https://doi.org/10.1002/qj.2445>.

524 Kulie, M. S., R. Bennartz, T. J. Greenwald, Y. Chen, and F. Weng, 2010: Uncertainties in  
525 microwave properties of frozen precipitation: implications for remote sensing and data  
526 assimilation. *J. Atmos. Sci.*, **67**, 3471-3487, <https://doi.org/10.1175/2010JAS3520.1>.

527 Liu, G., 2008: A database of microwave single-scattering properties for nonspherical ice  
528 particles. *Bull. Amer. Meteor. Soc.*, **89**, 1563-1570, [https://doi.org/10.1175/  
529 2008BAMS2486.1](https://doi.org/10.1175/2008BAMS2486.1).

530 Ma, Y., Z. Xiaolei, and F. Weng, 2017: Potential applications of small satellite microwave  
531 observations for monitoring and predicting global fast-evolving weathers. *IEEE J. of Sel.*  
532 *Top. Appl. Earth Obs. Remote Sens.*, **10**, 2441-2551, [https://doi.org/10.1109/](https://doi.org/10.1109/JSTARS.2017.2663335)  
533 [JSTARS.2017.2663335](https://doi.org/10.1109/JSTARS.2017.2663335).

534 Molod, A., L. Takacs, M. Suarez, J. Bacmeister, I.-S. Song, and A. Eichmann, 2012: The GEOS-  
535 5 Atmospheric General Circulation Model: Mean climate and development from  
536 MERRA to Fortuna. NASA Technical Report Series on Global Modeling and Data  
537 Assimilation, NASA TM-2012-104606, Vol. 28, 117 pp.

538 Nowell, H., G. Liu, and R. Honeyager, 2013: Modeling the single-scattering properties of  
539 aggregate snowflakes. *J. Geophys. Res.: Atmos.*, **118**, 7873-7885, [https://doi.org/10.1002/](https://doi.org/10.1002/jgrd.50620)  
540 [jgrd.50620](https://doi.org/10.1002/jgrd.50620).

541 Reising, S. C., T. C. Gaier, S. Padmanabhan, B. H. Lim, C. Heneghan, C. D. Kummerow, W.  
542 Berg, V. Chandrasekar, C. Radhakrishnan, S. T. Brown, J. Carvo and M. Pallas, “An  
543 Earth Venture In-Space Technology Demonstration Mission for Temporal Experiment  
544 for Storms and Tropical Systems (TEMPEST),” In: *Proc. 2018 IEEE International*  
545 *Geoscience and Remote Sensing Symposium (IGARSS 2018)*, Valencia, Spain, Jul. 2018,  
546 pp. 6301-6303, <https://doi.org/10.1109/IGARSS.2018.8517330>.

547 Rodgers, C. D., 2000: *Inverse Methods for Atmospheric Sounding: Theory and Practice*. World  
548 Science, 240 pp.

549 Schulte, R. M., and C. D. Kummerow, 2019: An optimal estimation retrieval algorithm for  
550 microwave humidity sounding channels with minimal scan position bias. *J. Atmospheric*  
551 *Ocean. Technol.*, **36**, 409-425, <https://doi.org/10.1175/JTECH-D-18-0133.1>.

552 Wentz, F. J., 1997: A well-calibrated ocean algorithm for special sensor microwave / imager. *J.*  
553 *Geophys. Res.*, **102**, 8703-8718, <https://doi.org/10.1029/96JC01751>.  
554 Wilheit, T. T., and A. T. C. Chang, 1980: An algorithm for retrieval of ocean's surface and  
555 atmospheric parameters from the observations of the scanning multichannel microwave  
556 radiometer. *Radio Sci.*, **15**, 525-544, <https://doi.org/10.1029/RS015i003p00525>.  
557

558 Table 1. Selected sensor specifications for TEMPEST-D and MHS.  
 559

	<b>TEMPEST-D</b>	<b>MHS</b>
<b>Channel Freq. (GHz)</b>	87, 164, 174, 178, 181	89, 157, 183±1, 183±3, 190
<b>Mass</b>	3.8 kg	63 kg
<b>Power</b>	6.5 W	74 W
<b>Altitude</b>	400 km	820 km
<b>Resolution at Nadir</b>	12.5 km (25 km at 87 GHz)	15.9 km
<b>NEDT (K)</b>	0.2, 0.3, 0.4, 0.4, 0.7	0.22, 0.34, 0.46, 0.40, 0.51
<b>Integration Time</b>	5 ms	18.5 ms

560  
 561  
 562 Table 2. Error statistics for TEMPEST-D retrieved values from Dec. 8-14, 2018 compared to  
 563 near-coincident MiRS values from the MetOp-A, MetOp-B, and NOAA-19 satellites. Bias  
 564 values are TEMPEST-D minus MiRS.  
 565

	<b>TPW</b>	<b>LWP</b>
<b>Correlation Coefficient</b>	0.976	0.692
<b>Bias</b>	-1.63 mm	-0.72 g/m <sup>2</sup>
<b>Standard Deviation</b>	2.87 mm	49.01 g/m <sup>2</sup>

566

567 **LIST OF FIGURES**

568 **Fig. 1.** Conceptual illustration of a TEMPEST train of CubeSats.

569 **Fig. 2.** Sample forward model error covariance ( $\mathbf{S}_y$ ) matrices, for the SST bins 275-276 K and  
570 300-301 K, and EIA bins 0-4 and 52-56 degrees. Values are given as the square root of the  
571 covariances so as to have units of Kelvin. Negative covariances are shown as -1 times the square  
572 root of the absolute value of the covariance. The square-root covariances are shown for the five  
573 radiometer channels centered at 87, 164, 174, 178 and 181 GHz, respectively.

574 **FIG. 3.** Median TEMPEST-D observed  $T_b$  minus forward model simulated  $T_b$  from ERA5, for  
575 all TEMPEST-D orbits from Dec. 8-14, 2018 and as a function of EIA and SST. The contour  
576 lines are plotted in increments of 0.25 K. These offsets are applied to simulated  $T_b$  in the  
577 retrieval algorithm before the simulated  $T_b$  are compared with the observed ones.

578 **Fig. 4.** TPW, LWP, and IWP retrieved from the TEMPEST-D and Metop-B satellites for a  
579 coincident overpass near 11:25 UTC on December 9, 2018. In the top panels, the retrieved  
580 TEMPEST-D fields from the CSU 1DVAR retrieval algorithm are plotted on top of the MetOp-  
581 B retrieved values, and in the bottom panels the Metop-B values from MiRS are plotted on top.

582 **Fig. 5.** Scatterplot comparing MiRS TPW from the MHS instrument on MetOp-B to TPW  
583 retrieved from TEMPEST-D, for all coincident observations from Dec. 8-14, 2018. Data have  
584 been gridded with a quarter-degree resolution, and observations are counted as coincident if they  
585 occur at the same grid point within 5 minutes of each other. The red line is the one-to-one line.

586 **FIG. 6.** As in Fig. 5, but for LWP.

587 **Fig. 7.** Mean difference between retrieved TPW and ERA5 reanalysis TPW as a function of earth  
588 incidence angle for the period Dec. 8-13, 2018 from the MiRS retrieval run on MetOp-B satellite

589 data (blue) and from the CSU 1DVAR retrieval run on TEMPEST-D satellite data (red). The  
590 overall mean bias between each retrieval and ERA5 has been removed.

591 **Fig. 8.** The blue line shows all TEMPEST-D retrieved values of TPW (top) and LWP (bottom)  
592 from Jan. 30, 2019, near 0600 UTC and within 10 km of the point (50.17°S, 33.25°E), as a  
593 function of EIA. The solid red line represents the corresponding single value retrieved from a  
594 near-coincident observation by MHS, with the red dashed lines representing +/- 1 standard  
595 deviation, as reported by the posterior covariance matrix.

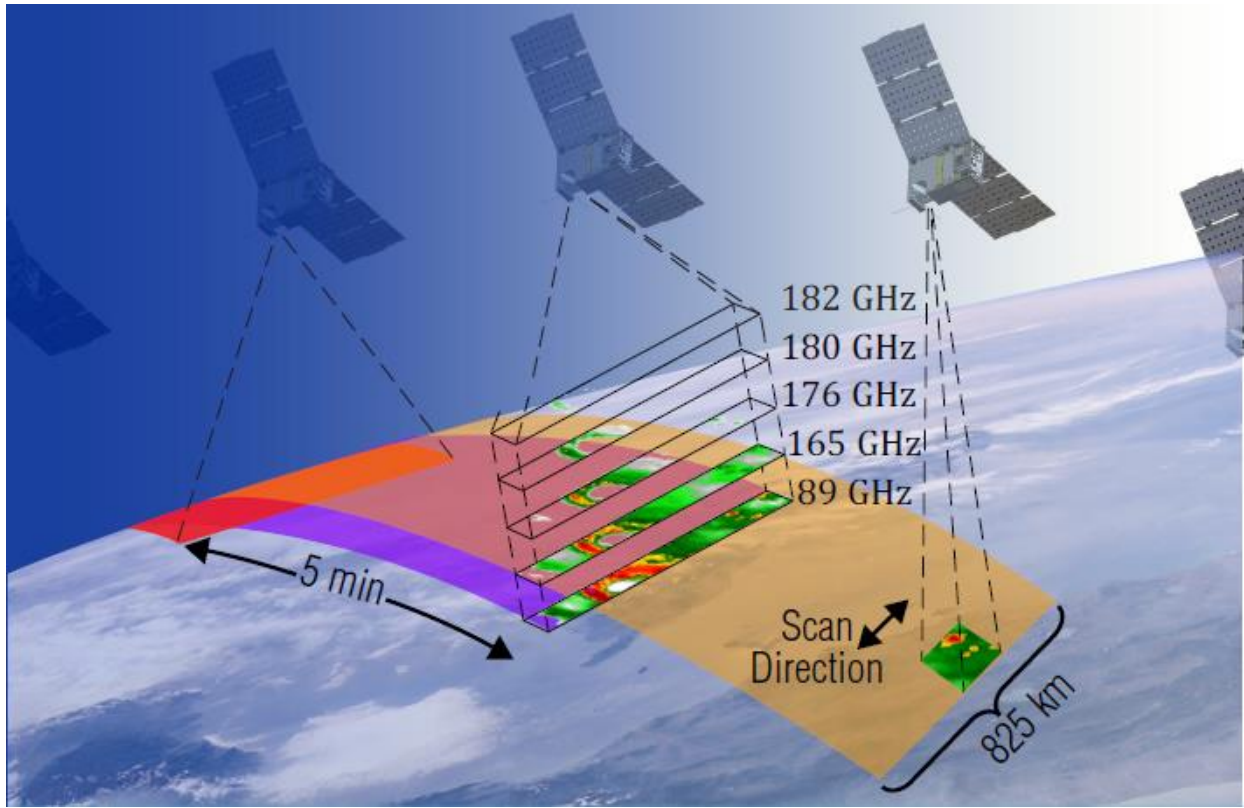
596 **Fig. 9.** (Top left) TPW retrieved by the CSU 1DVAR algorithm for an MHS overpass from  
597 MetOp-B over the Southern Ocean on Jan. 30, 2019 around 0600 UTC. The red line shows the  
598 ground track of a coincident TEMPEST-D overpass, while the TEMPEST-D satellite was in  
599 along-track scanning mode. The black 'X' shows the location of the MHS pixel used as a  
600 comparison point in Fig. 8. (Middle left) All of the TEMPEST-D pixels within 10 km of the  
601 TEMPEST-D ground track, plotted with respect to longitude and EIA. The color of each dot  
602 represents the magnitude of TPW retrieved. (Bottom left) The solid blue line is the TPW  
603 retrieved by TEMPEST-D at nadir along the ground track, with the shading showing the full  
604 range of values retrieved for the corresponding pixel at all view angles. The green line is the  
605 value retrieved at the closest MHS pixel, with shading representing +/- 1 standard deviation, as  
606 reported by the posterior covariance matrix. The plots on the right are similar, but for LWP  
607 instead of TPW.

608 **Fig. 10.** (Left) Median difference between TPW retrieved by TEMPEST-D at a given location  
609 and the TPW retrieved at the same location when the instrument was looking at nadir, for all yaw  
610 maneuver observations in the data record with latitudes between 45°S and 45°N. Observations  
611 are considered co-located if the centers of their respective instantaneous fields of view (IFOVs)

612 are within 5 km of each other. Results are shown for the full retrieval (with both forward model  
613 offsets and an  $\mathbf{S}_y$  matrix that depend on EIA and SST), for the retrieval with no EIA or SST  
614 dependent error assumptions at all, for the retrieval with EIA (but not SST) dependent  $\mathbf{S}_y$  and  
615 offsets, and for the retrieval with EIA and SST dependent offsets, but constant  $\mathbf{S}_y$ . (Right) The  
616 same type of plot, but for LWP. The y-axis is in terms of percentage difference because of the  
617 wide range of values possible for LWP.

618

619

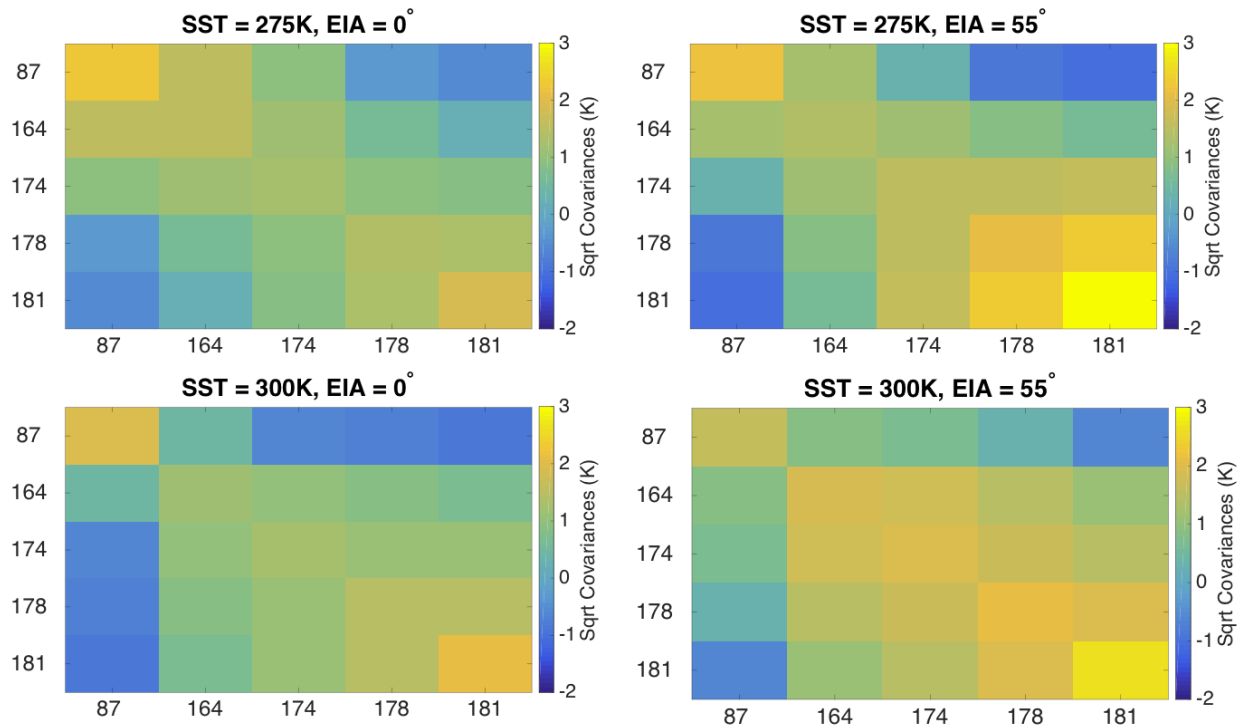


620

621 FIG. 1. Conceptual illustration of a TEMPEST train of CubeSats.

622

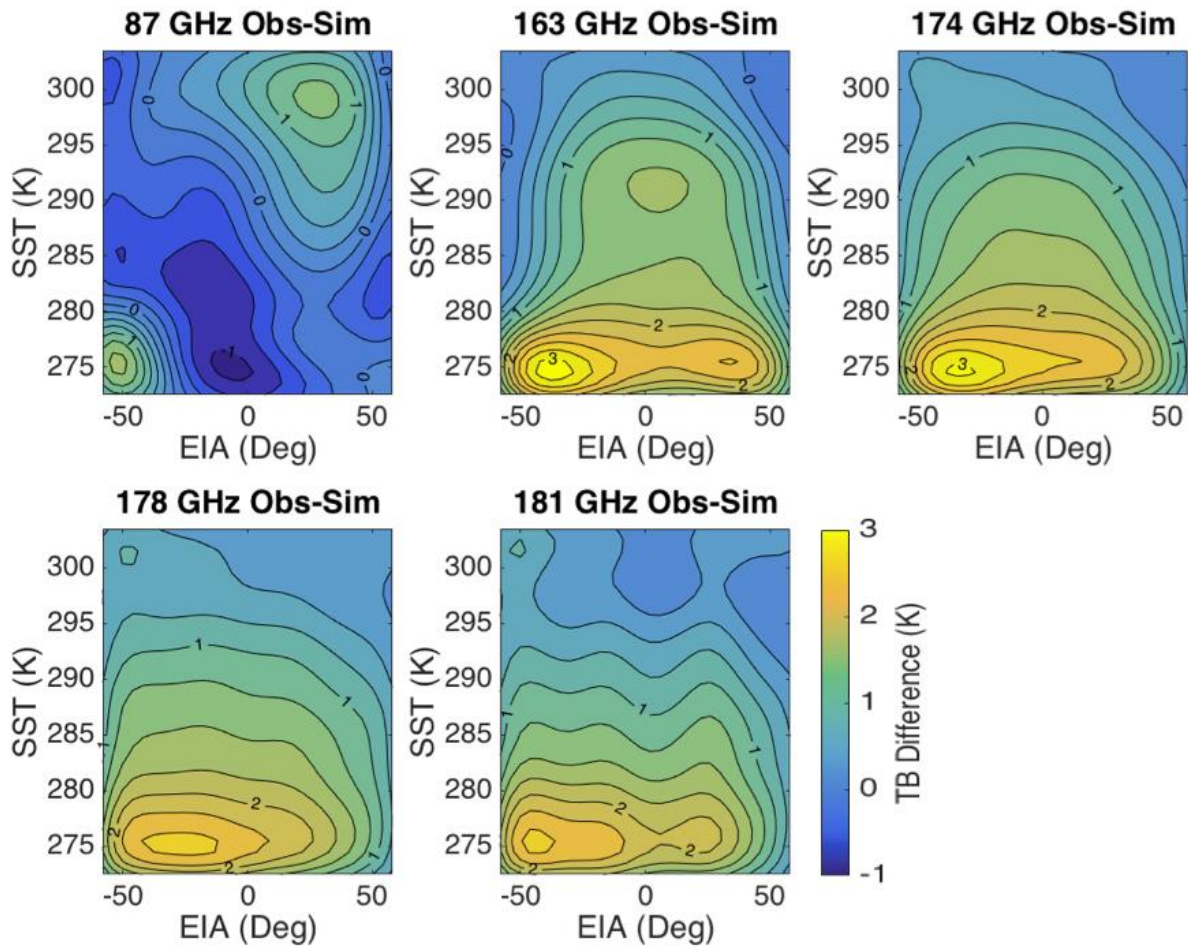
## Sample Error Covariance Matrices



623

624 FIG. 2. Sample forward model error covariance ( $\mathbf{S}_y$ ) matrices, for the SST bins 275-276 K and  
 625 300-301 K, and EIA bins 0-4 and 52-56 degrees. Values are given as the square root of the  
 626 covariances so as to have units of Kelvin. Negative covariances are shown as -1 times the square  
 627 root of the absolute value of the covariance. The square-root covariances are shown for the five  
 628 radiometer channels centered at 87, 164, 174, 178 and 181 GHz, respectively.

## Forward Model Offsets



629

630 FIG. 3. Median TEMPEST-D observed  $T_b$  minus forward model simulated  $T_b$  from ERA5, for

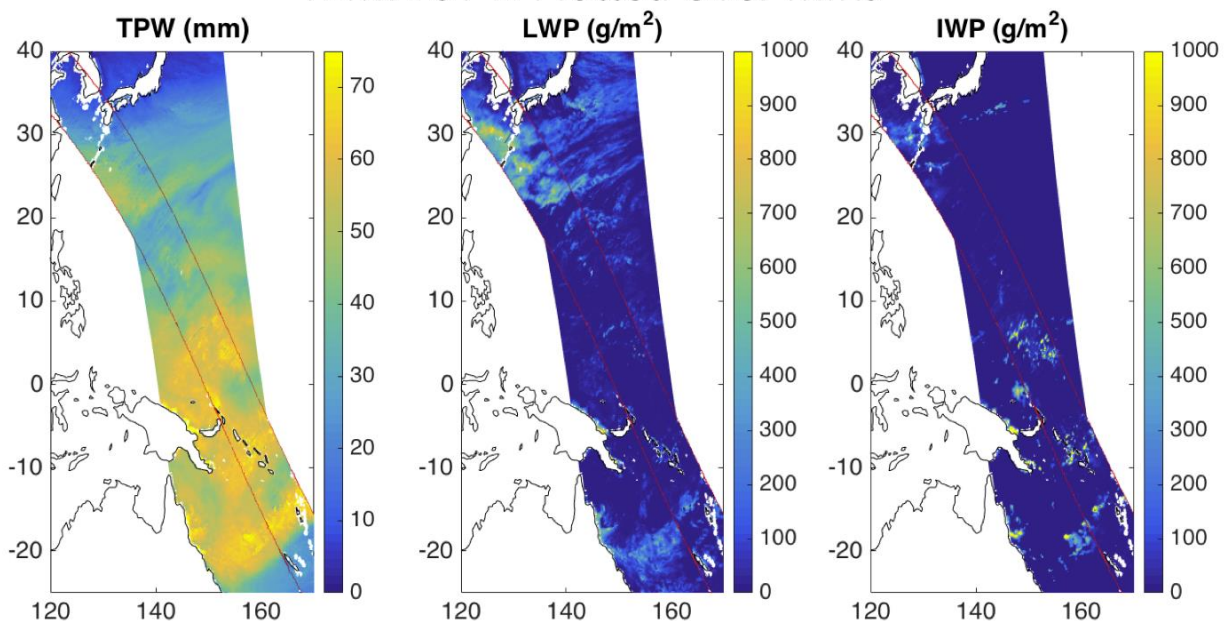
631 all TEMPEST-D orbits from Dec. 8-14, 2018 and as a function of EIA and SST. The contour

632 lines are plotted in increments of 0.25 K. These offsets are applied to simulated  $T_b$  in the

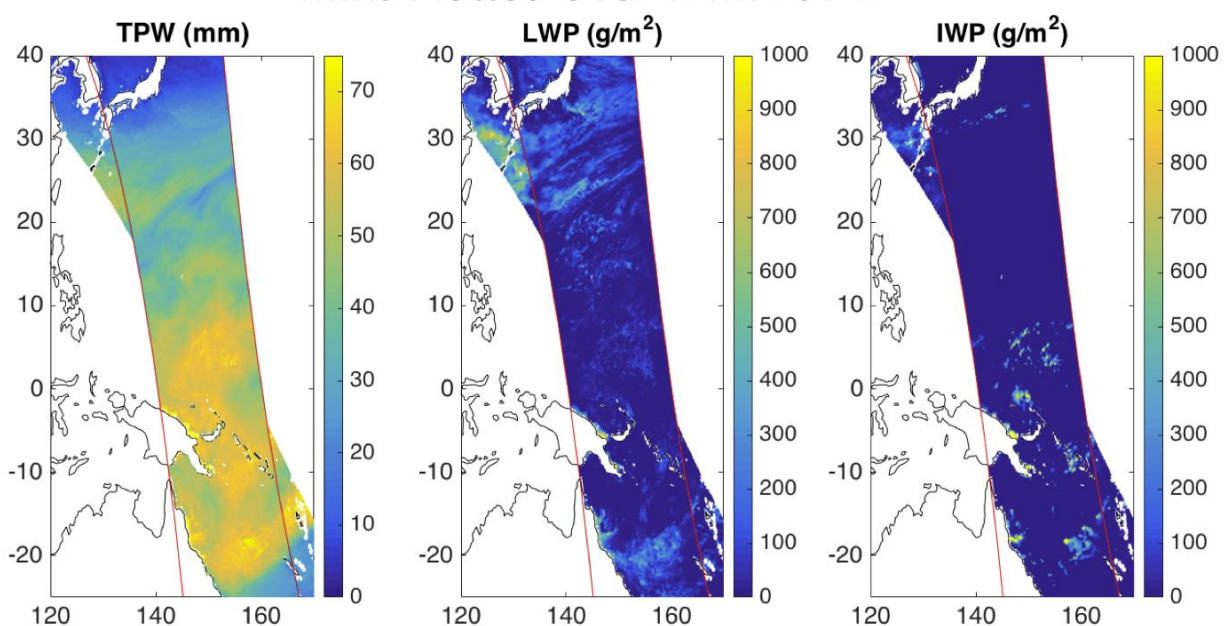
633 retrieval algorithm before the simulated  $T_b$  are compared with the observed ones.

634

## TEMPEST-D Plotted Over MiRS

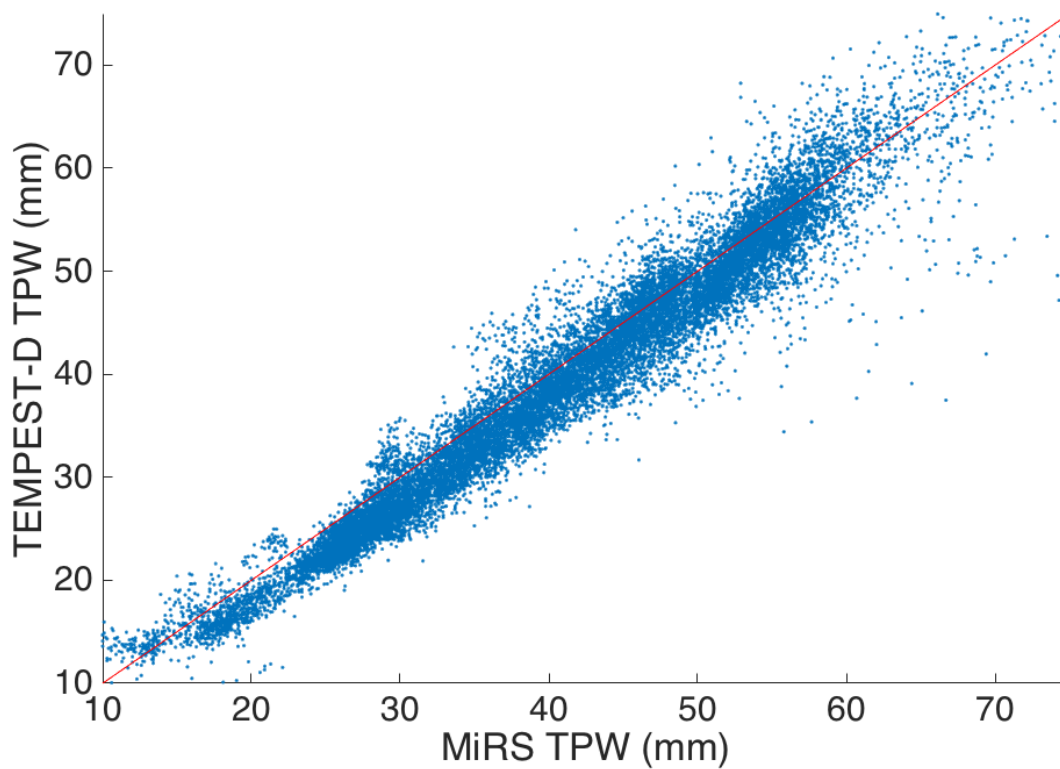


## MiRS Plotted Over TEMPEST-D

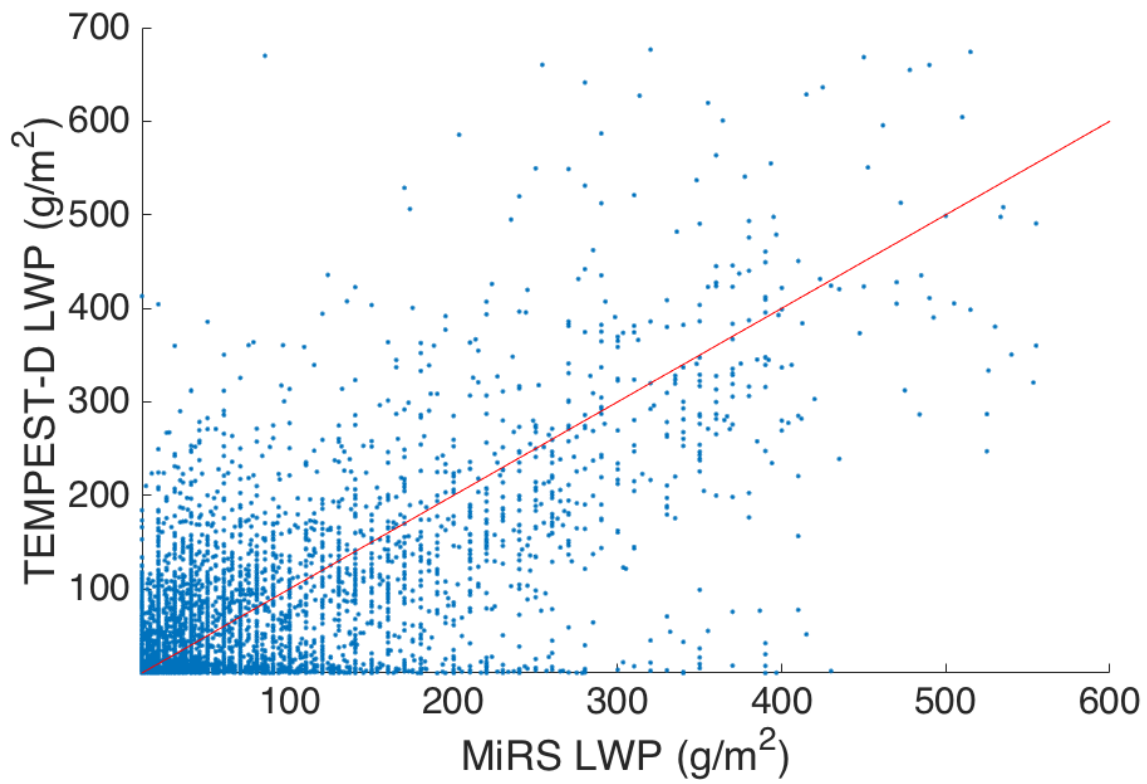


635

636 FIG. 4. TPW, LWP, and IWP retrieved from the TEMPEST-D and Metop-B satellites for a  
637 coincident overpass near 11:25 UTC on December 9, 2018. In the top panels, the retrieved  
638 TEMPEST-D fields from the CSU 1DVAR retrieval algorithm are plotted on top of the MetOp-  
639 B retrieved values, and in the bottom panels the Metop-B values from MiRS are plotted on top.



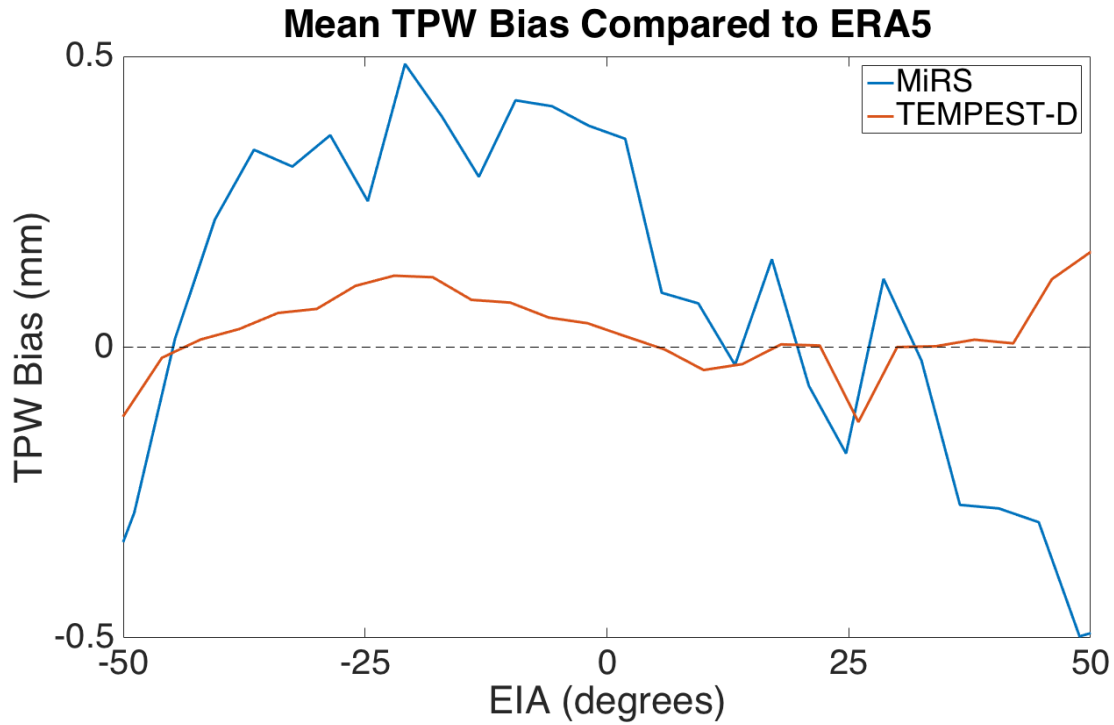
640  
641 FIG. 5. Scatterplot comparing MiRS TPW from the MHS instruments on MetOp-A, MetOp-B,  
642 and NOAA-19 to TPW retrieved from TEMPEST-D, for all coincident observations (n=17,869)  
643 from Dec. 8-14, 2018. Data have been gridded with a quarter-degree resolution, and observations  
644 are counted as coincident if they occur at the same grid point within 5 minutes of each other. The  
645 red line is the one-to-one line.



646

647 FIG. 6. As in Fig. 5, but for LWP.

648

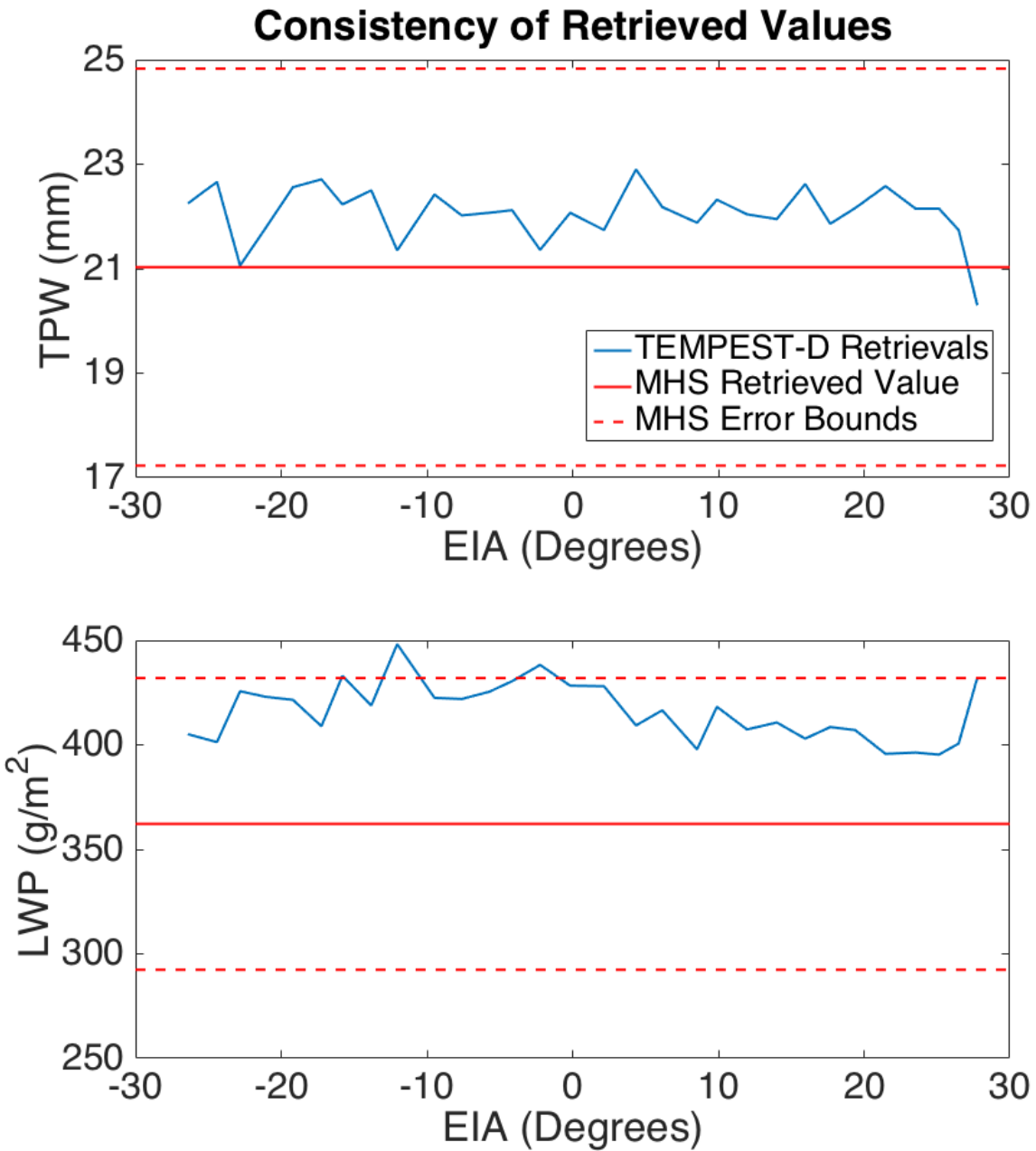


649

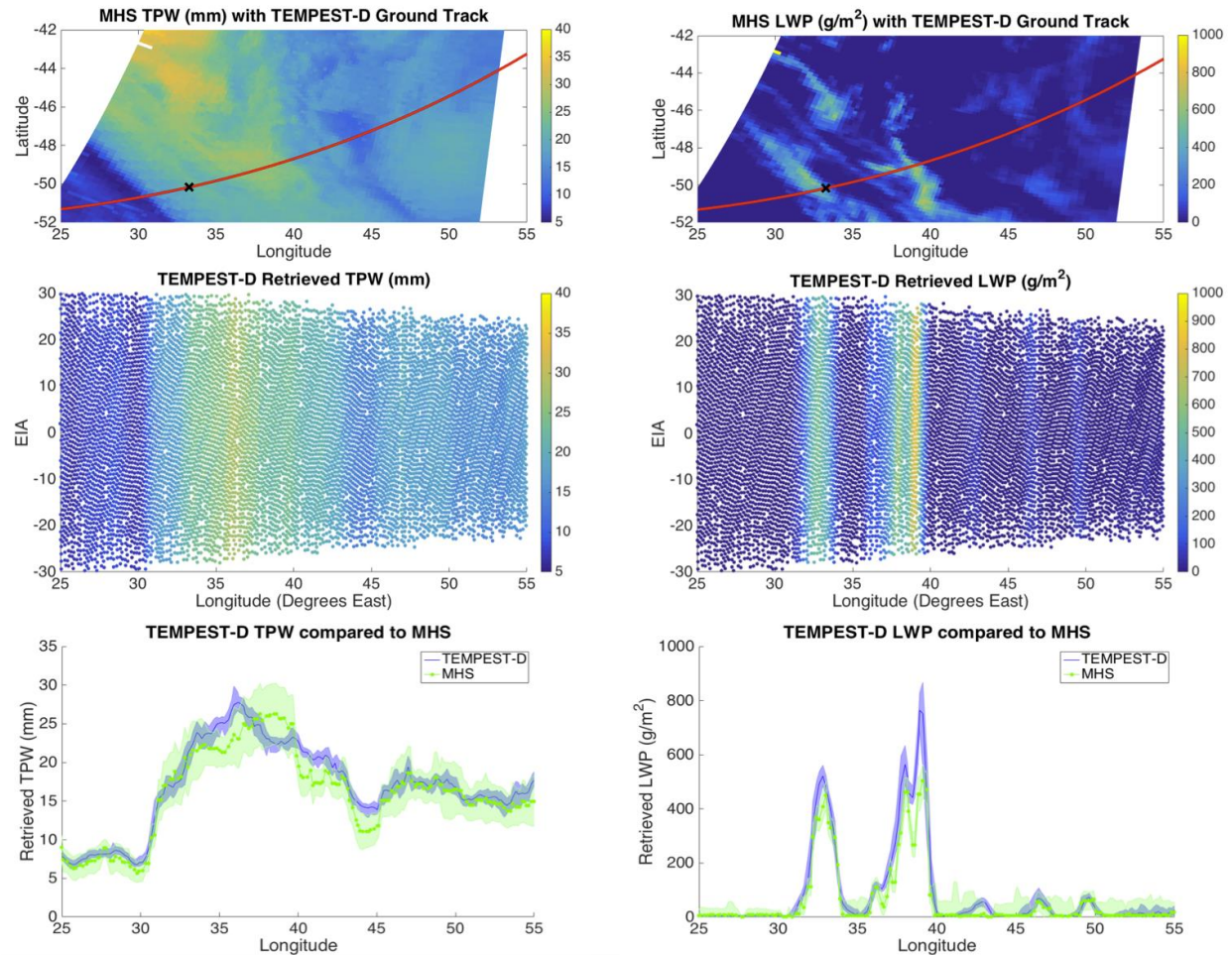
650 FIG. 7. Mean difference between retrieved TPW and ERA5 reanalysis TPW as a function of  
 651 earth incidence angle for the period Dec. 8-14, 2018 from the MiRS retrieval run on MetOp-B  
 652 satellite data (blue) and from the CSU 1DVAR retrieval run on TEMPEST-D satellite data (red).

653 The overall mean bias between each retrieval and ERA5 has been removed.

654



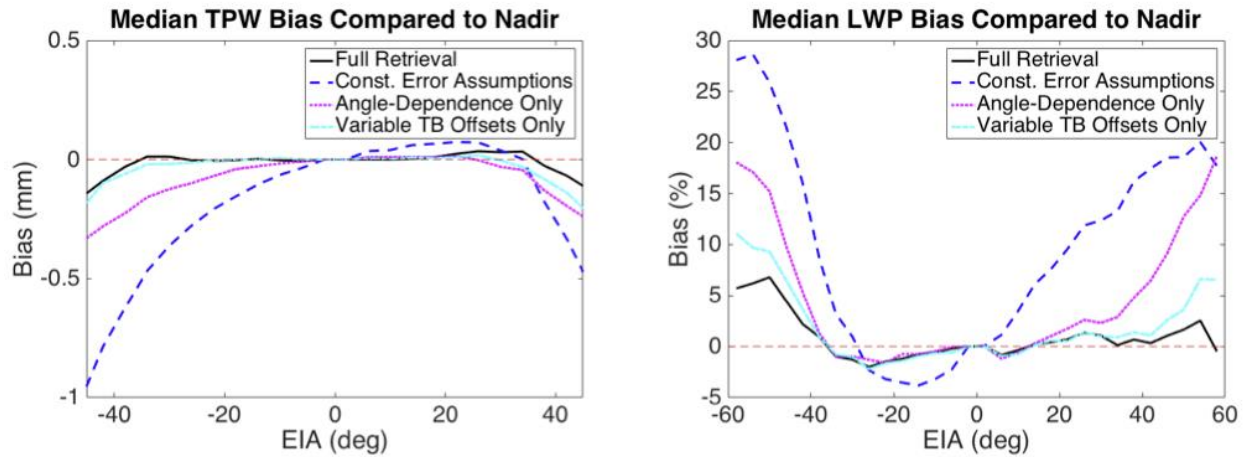
655  
 656 FIG. 8. The blue line shows all TEMPEST-D retrieved values of TPW (top) and LWP (bottom)  
 657 from Jan. 30, 2019, near 0600 UTC and within 10 km of the point (50.17°S, 33.25°E), as a  
 658 function of EIA. The solid red line represents the corresponding single value retrieved from a  
 659 near-coincident observation by MHS, with the red dashed lines representing  $\pm 1$  standard  
 660 deviation, as reported by the posterior covariance matrix.



661

662 FIG. 9. (Top left) TPW retrieved by the CSU 1DVAR algorithm for an MHS overpass from  
 663 MetOp-B over the Southern Ocean on Jan. 30, 2019 around 0600 UTC. The red line shows the  
 664 ground track of a coincident TEMPEST-D overpass, while the TEMPEST-D satellite was in  
 665 along-track scanning mode. The black 'X' shows the location of the MHS pixel used as a  
 666 comparison point in Fig. 8. (Middle left) All of the TEMPEST-D pixels within 10 km of the  
 667 TEMPEST-D ground track, plotted with respect to longitude and EIA. The color of each dot  
 668 represents the magnitude of TPW retrieved. (Bottom left) The solid blue line is the TPW  
 669 retrieved by TEMPEST-D at nadir along the ground track, with the shading showing the full  
 670 range of values retrieved for the corresponding pixel at all view angles. The green line is the  
 671 value retrieved at the closest MHS pixel, with shading representing +/- 1 standard deviation, as

672 reported by the posterior covariance matrix. The plots on the right are similar, but for LWP  
673 instead of TPW.



674

675 FIG. 10. (Left) Median difference between TPW retrieved by TEMPEST-D at a given location  
 676 and the TPW retrieved at the same location when the instrument was looking at nadir, for all yaw  
 677 maneuver observations in the data record with latitudes between 45°S and 45°N. Observations  
 678 are considered co-located if the centers of their respective instantaneous fields of view (IFOVs)  
 679 are within 5 km of each other. Results are shown for the full retrieval (with both forward model  
 680 offsets and an  $S_y$  matrix that depend on EIA and SST), for the retrieval with no EIA or SST  
 681 dependent error assumptions at all, for the retrieval with EIA (but not SST) dependent  $S_y$  and  
 682 offsets, and for the retrieval with EIA and SST dependent offsets, but constant  $S_y$ . (Right) The  
 683 same type of plot, but for LWP. The y-axis is in terms of percentage difference because of the  
 684 wide range of values possible for LWP.

685